ChemComm

Nanoelectrochemistry at Liquid/Liquid Interfaces for Analytical, Biological, and Material Applications

Journal:	*ChemComm*
Manuscript ID	CC-FEA-04-2023-001982.R1
Article Type:	Feature Article

FEATURE ARTICLE

Nanoelectrochemistry at Liquid/Liquid Interfaces for Analytical, Biological, and Material Applications

Received 00th January 20xx,
Accepted 00th January 20xx

DOI: 10.1039/x0xx00000x

Siao-Han Huang,[a] Moghitha Parandhaman,[a] Solaleh Farnia,[b] Jiyeon Kim,*[b] and Shigeru Amemiya*[a]

Herein, we feature our recent efforts toward the development and application of nanoelectrochemistry at liquid/liquid interfaces, which are also known as interfaces between two immiscible electrolyte solutions (ITIES). Nanopipets, nanopores, and nanoemulsions are developed to create the nanoscale ITIES for the quantitative electrochemical measurement of ion transfer, electron transfer, and molecular transport across the interface. The nanoscale ITIES serves as an electrochemical nanosensor to enable the selective detection of various ions and molecules as well as high-resolution chemical imaging based on scanning electrochemical microscopy. The powerful nanoelectroanalytical methods will be useful for biological and material applications as illustrated by in-situ studies of solid-state nanopores, nuclear pore complexes, living bacteria, and advanced nanoemulsions. These studies provide unprecedented insights into the chemical reactivity of important biological and material systems even at the single nanostructure level.

1. Introduction

Electrochemistry at liquid/liquid interfaces has a history of more than a century to be well-recognized in both fundamental and applied electrochemistry.[1, 2] A liquid/liquid interface is also known as an interface between two immiscible electrolyte solutions (ITIES) in electrochemistry.[3] The electrolytes ensure ionic conductivity to enable the accurate control and measurement of potential drop and current flow across the interface. Specifically, ions can be transferred across the interface to control the phase boundary potential in potentiometry[4] or generate a current response in amperometry and voltammetry.[5] Electrons can be also transferred across the interface between redox molecules dissolved in opposite phases. Fundamentally, Marcus theories were developed to describe the kinetics of both ion-transfer[6] (IT) and electron-transfer[7, 8] (ET) reactions at liquid/liquid interfaces. The IT theory was originally inspired by the molecular dynamics simulation of water fingers[9] and was assessed experimentally.[10, 11] Interestingly, an inverted region was predicted by the ET theory at liquid/liquid interfaces in contrast to metal/solution interfaces[12] and was tested experimentally by employing scanning electrochemical microscopy (SECM).[13]

This article features our recent efforts toward the development and application of nanoelectrochemistry at liquid/liquid interfaces. Earlier studies were reviewed a decade ago to highlight the fundamental electrochemistry of IT and ET reactions at the nanoscale ITIES.[14, 15] During the last decade, remarkable progress was made to advance the nanoelectrochemical methods based on the ITIES as reliable and quantitative analytical tools for biological and material research. Biological applications are illustrated by in-situ studies of nucleocytoplasmic molecular transport and bacterial physiology. Advanced nanoemulsions (NEs) and solid-state nanopores were also studied as soft and hard nanomaterials, respectively, at the single nanostructure level for chemical sensing. These studies provided unprecedented chemical information that is unobtainable by ex-situ or ensemble studies.

It should be emphasized that the importance of nanoelectrochemistry at liquid/liquid interfaces is represented by the number of recent reviews, which are complementary to this feature article. For instance, a recent fundamental review critically assessed theoretical and experimental studies to discuss the structure and thickness of liquid/liquid interfaces.[16] Moreover, experimental and theoretical foundations were reviewed to employ liquid/liquid interfaces for “impact experiments,”[17] which are also known as single-entity[18] or single-particle[19] electrochemistry as introduced in Section 2.3. By contrast, recent reviews featured the biological application of nanoelectrochemical methods based on liquid/liquid interfaces to reveal the dynamics of neurotransmitter exocytosis at the single-synaptic level.[20, 21] Another recent review introduced the application of liquid/liquid interfaces for electrocatalysis and photoelectrocatalysis as mediated by various nanomaterials and redox enzymes.[22]

2. Nanoelectroanalytical Methods

Here, we aim at discussing the working principles of three powerful electroanalytical methods based on the nanoscale ITIES. A key takeaway is that these methods were significantly reinforced as reproducible and quantitative methods to enable various

---

[a] Department of Chemistry, University of Pittsburgh, Pittsburgh, PA, 15260, USA. E-mail: amemiya@pitt.edu.
[b] Department of Chemistry, University of Rhode Island, Kingston, RI, 02881, USA. E-mail: jkim25@uri.edu.

† Footnotes relating to the title and/or authors should appear here.

Electronic Supplementary Information (ESI) available: [details of any supplementary information available should be included here]. See DOI: 10.1039/x0xx00000x applications as introduced in Sections 3–6. Specifically, nanoscale liquid/liquid interfaces can be formed reproducibly and reliably at the tip of a well-characterized nanopipet. The use of nanopipet-supported liquid/liquid interfaces as SECM nanotips enables high-resolution electrochemical imaging.[23, 24] More recently, single-particle electrochemistry[19] allowed for studies of IT, ET, and molecular transport at single NEs as the new form of the nanoscale ITIES.

2.1. Nanopipet-Supported ITIES

A nanometer-sized liquid/liquid interface can be formed at the tip of a nanopipet (Fig. 1A) to find various sensing applications. Nanopipet-supported ITIES is advantageous for the electrochemical detection of redox-inactive ions, e.g., neurotransmitters, acetylcholine and tryptamine,[25] and bacterial metabolites, lactate[26] and CO_3^{2-}.[27] The selectivity and sensitivity of these ITIES-based nanosensors were high enough for practical applications to detect the target ions in complicated biological media around living neuronal cells[28, 29] and bacteria.[26, 27] Moreover, nanopipet-supported ITIES was applied for fundamental studies to measure fast ion-transfer kinetics[10, 11] and electrodeposit metal nanoparticles[30] at the nanoscale interface.

Experimentally, a nanopipet is usually filled with a water-immiscible organic solution of highly lipophilic electrolytes and immersed in an aqueous electrolyte solution to form a nanometer-sized interface. A metal electrode is inserted into the organic phase to externally control the interfacial potential against an aqueous reference electrode and measure the current based on interfacial charge transfer. For instance, a more negative potential is applied to accelerate the transfer of cations from the aqueous phase to the organic phase. With a sufficiently negative potential, the resultant ionic current is limited by the steady-state diffusion of the transferred cations from the aqueous solution to the interface as given by

$$i_{T,\infty} = 4xzFD_w c_0 a \qquad (1)$$

where x is a function of RG[31] (= r_g/a = 1.4 in this study; a and r_g are the inner and outer radii of a micropipet tip), z is the charge of a transferred ion, F is the Faraday constant, and c_0 is its concentration. The transferred cations efficiently diffuse away into the organic phase through the tapered region of the nanopipet to yield a steady-state cyclic voltammogram. By contrast, a reverse peak current is expected at the micropipet-supported interface.[32] Experimental cyclic voltammograms at nanopipet and micropipets are illustrated later.

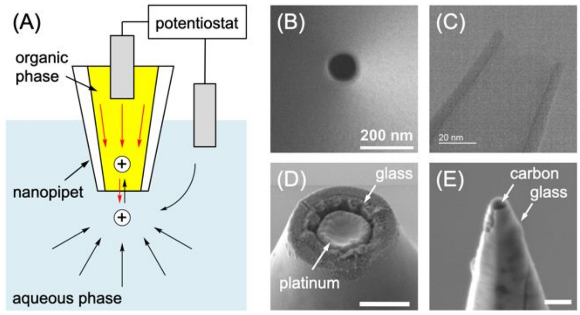

Fig. 1 (A) Scheme of IT voltammetry/amperometry at (A) the nanopipet-supported ITIES. Reproduced from Ref. 5 with permission from Elsevier. (B) SEM image of a quartz nanopipet coated with a 3 nm-thick Au film. Reproduced from Ref. 33 with permission from the American Chemical Society. (C) TEM image of an as-pulled quartz nanopipet. Reproduced from Ref. 34 with permission from the American Chemical Society. SEM images of damaged (D) Pt and (E) carbon nanoelectrodes with scale bars of 1 μm and 200 nm, respectively. Reproduced from Refs. 35 and 36 with permission from the American Chemical Society and the Electrochemical Society, respectively.

Several issues were identified and overcome to reproducibly form a nanopipet-supported liquid/liquid interface for reliable current measurements. A nanopipet with a tip diameter of down to 10 nm can be reproducibly obtained by heat-pulling a glass or quartz capillary using a computer-controlled CO_2-laser puller.[37] The reproducible tip size was confirmed when a nanopipet was coated with a 3 nm-thick metal layer and inspected by scanning electron microscopy (SEM; Fig. 1B[33]) or was directly imaged by transmission electron microscopy (TEM; Figure 1C[34]). In TEM, the electron-beam intensity must be optimized to prevent the melt of the insulating nanopipet tip. A stable ITIES is spontaneously and reproducibly formed at the tip of a nanopipet to minimize the contact area between the mutually immiscible solutions when the inner wall of the organic-filled pipet is sufficiently hydrophobic. The wall of a nanopipet can be reproducibly rendered hydrophobic by reacting under a dry atmosphere with *N*,*N*-dimethyltrimethylsilylamine as a silanization reagent with high purity and moderate reactivity.[38] The excessive reaction of the glass tip with a highly reactive and less pure silanization reagent under a wet atmosphere can form a polymeric material to block the tip end.[10] A recent study also demonstrated that the nanopipet-supported ITIES was protected from adventitious contaminants from the metal electrode in the organic phase and from ambient air to obtain reproducible current responses.[27]

2.2. Nanoscale SECM

Nanopipet-supported liquid/liquid interfaces played crucial roles in the recent development and applications of nanoscale SECM.[24] For instance, nanopipet-supported ITIES tips were applied to SECM imaging of single nanopores[34, 39] (see Sections 3.1) as well as single bacteria.[26] The recent SECM study of single bacteria employed a nanopipet-supported ITIES tip as a lactate nanosensor to visualize the metabolic interaction between two human oral microbiomes, i.e., *Streptococcus mitis* and *Corynebacterium matruchotii*, through lactate production and consumption at a single-cell level. Moreover, a nanopipet-supported ITIES tip was positioned at a nanometer distance from living *Aplysia neurons* by using SECM to quantitatively monitor the release dynamics and concentration of acetylcholine with millisecond temporal resolution.[28] The acetylcholine sensing nanoprobe was combined with SECM also to reveal the dynamics of Ca^{2+}-dependent acetylcholine exocytosis from a living neuronal soma.[29] The practical applications of nanoscale SECM for neuronal and bacterial systems were enabled by the high selectivity of the ITIES-based nanosensors for redox inactive acetylcholine and lactate, respectively, in complicated biological media.

Advantageously, a nanopipet-supported ITIES tip is robust in comparison with a solid nanoelectrode, which has been also employed for nanoelectrochemical measurements including nanoscale SECM. A solid nanoelectrode is an electronic conductor and is readily damaged by electrostatic charge, which had not been recognized or accepted despite decades-long research on solid nanoelectrodes.[40] Electrostatic charges may be injected from an operator to the contact wire of a nanoelectrode to completely damage the tip including the surrounding glass sheath. The resultant nanoscale damages were demonstrated for both platinum[35] and carbon[36] nanoelectrodes (Figs. 1D and 1E, respectively). In addition, electrostatic charges may be injected into a nanoelectrode from the operational amplifier of a potentiostat. The amplifier Is transiently saturated to generate a high voltage when the potentiostat is switched between the actual electrochemical cell and an internal dummy cell.[41] The respective sources of electrostatic charges can be eliminated by grounding the operator under high humidity and by maintaining the connection between the potentiostat and the electrochemical cell.[35, 42] The absence of the tip damage can be confirmed by SEM or TEM of a used nanoelectrode as demonstrated for Pt nanoelectrodes with sizes of down to ~200 nm.[42] Unfortunately, the inspection of smaller nanoelectrodes by SEM or TEM has been reported only before use.

Reproducible nanoscale SECM imaging was enabled by the precise positioning of a nanopipet-supported ITIES tip,[34, 39] which was robust enough to yield reproducible current responses (see Section 2.1). An SECM tip was moved vertically and laterally by using closed-loop piezo actuators with the sub-nanometer resolution based on capacitive feedback (Fig. 2), which dynamically stabilizes the stage positions. The sub-nanometer resolution also required the piezo actuators that were designed for relatively short travel distances of 50–100 µm and, subsequently, mounted on the micrometer stage with longer travel distances of 0.5–1 inches. The micromanipulators must be locked to minimize the nanoscale creeping or drift of the stage.[42, 43]

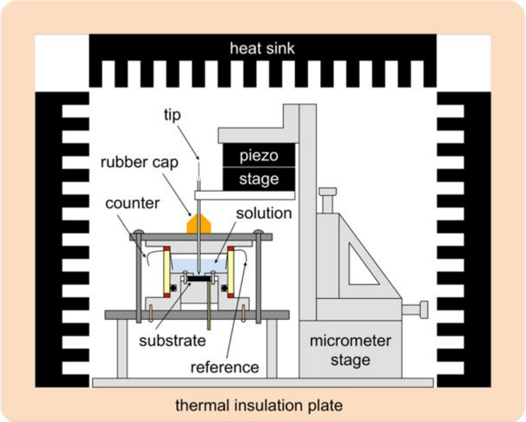

Fig. 2 Scheme of nanoscale SECM set up with an isothermal chamber. Reproduced from Ref. 44 with permission from the American Chemical Society.

Importantly, nanopipet-supported ITIES tips were used to identify the thermal drift of the tip position, which was minimized by developing an isothermal chamber for reproducible nanoscale SECM imaging.[45] An SECM tip must be positioned within the tip radius, *a*, from a substrate to investigate the reactivity and topography of the substrate with high spatial resolution. The short distance, however, is readily compromised by a change in the ambient temperature, which thermally expands or shrinks the SECM stage attached to a nanometer-sized tip (Fig. 2). The thermal drift can be minimized by isolating the SECM stage within an isothermal chamber, where the temperature changes only ~0.2 mK/minute. The chamber is made of vacuum-sealed thermal insulation plates to prevent heat exchange between the interior of the chamber and the external ambient. Moreover, extra heat is generated around the SECM stage by an operator and is quickly absorbed by the surrounding metallic heat sinks to thermally equilibrate the chamber interior. The remarkable stability of ~0.4 nm/min in the distance between the tip and the substrate was measurable by monitoring the ionic current at an extremely small nanopipet-supported liquid/liquid interface. The highly stable tip position also confirmed that the heat sources that were not eliminated by the isothermal chamber, e.g., reaction heat, were not relevant to the thermal drift of an SECM tip. The isothermal chamber was employed for SECM imaging of single nanopores[34, 39] and single nanoparticles.[42, 43] The isothermal chamber also enabled SECM-based nanogap voltammetry to investigate fast ET and adsorption reactions at carbon electrodes,[44] e.g., graphene,[46] highly oriented pyrolytic graphite,[47-49] and electron-beam-deposited carbon.[50, 51]

2.3. Single NE Detection

Single-entity electrochemistry[18] has emerged recently to enable the electrochemical detection of single NEs dispersed in an immiscible electrolyte solution.[52] Importantly, this general approach applies not only to simple oil-in or water-in emulsions but also to various "soft" nanoparticles including artificial liposomes,[53] human platelets,[54] and vesicles in the cytoplasm of single cells[55] in addition to Pickering emulsions,[56] which are practically used in cosmetic and culinary technologies. In these applications, the "soft" nanoparticles contained redox-active molecules, which were detected at the UME upon collision with each nanoparticle to generate a current spike as discussed below. Alternatively, the current response of a UME to redox-active species in the solution can be lowered by the collision of individual "soft" nanoparticles, which block the electrode surface.[57] This principle was applied for the detection of single living bacteria[58] and single virus.[59] By contrast, the current response of a UME to a redox-active species was enhanced by the collision of an individual virus, which was recognized by the antibody functionalized with glucose oxidase to regenerate the redox-active species.[60] The catalytic amplification was successfully applied to detect murine cytomegalovirus in the urine of infected mice.

Fundamentally, Bard pioneered the intriguing electrochemical strategy for single NE detection by encapsulating redox-active molecules in the NE to obtain a spike current response upon the collision of each NE with a metal ultramicroelectrode (UME).[52] The current response based on the electrolysis of the redox-active molecules at the UME increases upon collision and decays as the redox-active molecules are depleted in the NE. Importantly, the ET reaction at the emulsion/electrode interface must be coupled with another charge transfer reaction at the emulsion/solution interface to maintain the electroneutrality of the emulsions, e.g., an IT reaction at the emulsion/solution interface as an ITIES (Fig. 3).[61] The heterogeneous ET reaction was also coupled with a homogeneous ET reaction in the emulsion for the electrogenerated chemiluminescence detection of single emulsions as synchronized with current spikes.[62] The spike current based on the oxidation of decamethylferrocene at the emulsion/electrode interface was amplified by the immediate reduction of ferrocenium by $CO_2^{\bullet-}$ at the emulsion/solution.[63] The strong reducing reagent, $CO_2^{\bullet-}$, was generated from oxalate at the solution/electrode interface.

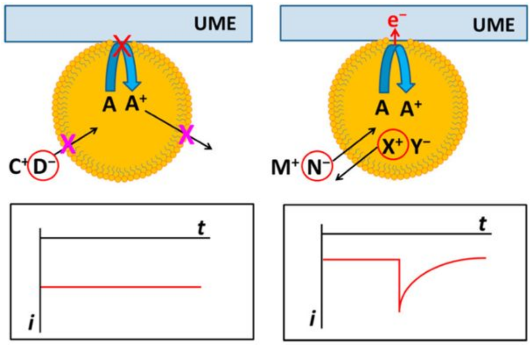

Fig. 3 Electrochemical detection of the single NE collided on the UME (left) only with a residual background current without the transfer of an ion, A^+ or D^-, across the emulsion/water interface or (right) with a current spike based on the oxidation of a redox probe, A, to A^+ as coupled with the transfer of an ion, X^+ or N^-, across the emulsion/water interface. The oil-in-water emulsion (yellow) is surrounded and stabilized by tadpole-shaped amphiphilic molecules. Reproduced from Ref. 61 with permission from the American Chemical Society.

Liquid/liquid interfaces can be used instead of UMEs to detect single NEs electrochemically.[64-66] Historically, Kakiuchi pioneered the electrochemical formation and detection of microemulsions at macroscopic liquid/liquid interfaces.[67] Chronoamperometric spikes were observed stochastically and attributed to the transfer of ~2.4 $\times$ 10^5 emulsions by assuming a radius of 1 μm and a surface charge density of 0.1 C/m^2. Recently, individual oil-in-water microemulsions were preformed in the aqueous phase and detected as current spikes at the ITIES.[68] The current spikes were attributed to the fusion of the single emulsion at the ITIES followed by the release of ions from the emulsion into the aqueous phase. The distribution of the emulsion diameter around 2 μm at the ITIES was estimated electrochemically from the charge under the current spike to satisfactorily agree with the emulsion diameter distribution in solution as determined by dynamic light scattering. This agreement ensures the high stability of the emulsions with minimal aggregation at the interface and in the solution. More recently, current spikes with ~10 μm-diameter emulsions were studied to suggest a change in the interfacial potential of the emulsions upon fusion with the ITIES.[69]

The reproducibility of current spikes in single NE detection is determined not only by the size distribution of NEs but also by the efficiency of electron transfer across the NE/UME junction or ion transfer across the NE/ITIES junction. Advantageously, these junctions are stable enough to mediate the exhaustive transfer of electrons and ions from or into the NEs[61] despite the relatively large NE diameters of >40 nm. Subsequently, a single current spike is observed upon the collision of each NE to correlate the collision frequency to the diffusion coefficient and concentration of NEs. Moreover, fast electron or ion transfer across the stable junctions narrows the current spike to maximize the current sensitivity, which is eventually limited by the number of available electrons and ions in the NE. By contrast, it is well known that the collision of single Ag nanoparticles at the UME can yield multiple current spikes to compromise the current sensitivity.[70] Specifically, Ag nanoparticles with diameters of >50 nm are only partially oxidized during each collision and are desorbed from the UME to rapidly bounce across the UME surface, thereby yielding multiple current spikes.

3. Solid-State Nanopore Membrane

The goal of this section is to discuss how ion transport through ultrathin nanoporous membranes can be investigated quantitatively by employing nanopipet- and micropipet-supported liquid/liquid interfaces as ion-selective SECM tips.[23] A major takeaway is that the powerful SECM method established a quantitative structure–permeability relationship for ultrathin nanoporous membranes. Significantly, this relationship is useful not only to better understand nucleocytoplasmic molecular transport (Section 4) but also to design highly sensitive ion sensors based on nanoscale ITIES arrays (Section 3.3). Specifically, the ultrathin nanoporous membranes can be molecularly thin (~10 nm in thickness) and, subsequently, much more permeable than traditional nanoporous membranes but are still robust enough to be self-standing in the solution.[71] The ultrathin nanoporous membranes can be considered as superior alternatives for hemodialysis[72] and cell co-culture[73] and also as enabling nanomaterials for wearable artificial kidney[74] and tissue-on-chips.[75] The dimensions of solid-state nanopore membranes can be similar to those of the nuclear envelope perforated by nuclear pore complexes with a pore length of 35 nm and a pore radius of 24 nm.[76]

3.1 Single Nanopore Imaging

The power of nanopipet-supported liquid/liquid interfaces as nanoscale SECM tips were demonstrated by imaging ion transport through single solid-state nanopores.[39] This work represented the first example of truly nanoscale SECM imaging with a spatial resolution of less than 100 nm with the substrate fully immersed in the solution. A much higher spatial resolution of ~1 nm was achieved earlier by imaging biological macromolecules on a mica substrate covered with a thin layer of condensed water (a few nanometers or less).[77] Specifically, a nanopipet-supported liquid/liquid interface was scanned over a nanoporous membrane by maintaining a short tip–substrate distance of ~1 nm in the isothermal chamber. The current based on the transfer of tetrabutylammonium (TBA^+) across the nanopipet-supported interface was enhanced when the tip was scanned over the nanopore. The high spatial resolution of ~30 nm was limited by the tip diameter of a nanopipet and was confirmed quantitatively by the finite element analysis of SECM images.

More recently, a nanopipet-supported liquid/liquid interface was employed as an SECM tip to image a periodic array of solid-state nanopores with uniform pore diameters of 100 nm (Fig. 4A).[34] The nanoporous membrane was imaged by using TEM to ensure the periodicity and diameter of nanopores. Nanoscale SECM imaged the periodicity of the nanoporous membrane (Figure 4B). The pore diameter in the SECM image was larger than the actual pore diameter owing to the lateral diffusion of TBA^+ in the gap between the tip and the pore. The diffusion effect was corrected by the finite element analysis of the SECM images to find that the pore diameter determined electrochemically in the electrolyte solution quantitatively agreed with the pore diameter determined by TEM in a vacuum. In contrast to the earlier study,[39] the tip diameter of a nanopipet was also determined by TEM (Fig. 1C) to ensure the reliability of the finite element analysis.

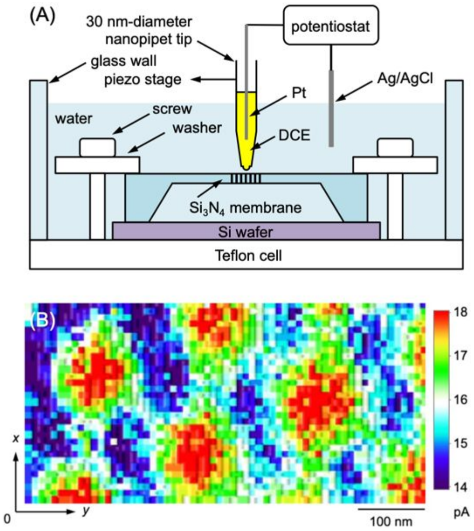

Fig. 4 (A) SECM cell with a nanoporous membrane and an organic-filled nanopipet tip. DCE represents 1,2-dichloroethane. (B) A 300 nm × 600 nm SECM image of single Si_3N_4 nanopores as obtained with a sphere-cap nanopipet tip in 1 M KCl containing 5 mM TBACl. Probe scan rate, 100 nm/s in the x direction. Reproduced from Ref. 34 with permission from the American Chemical Society.

The use of an IT reaction at the tip and the substrate is advantageous for high-resolution SECM imaging. When an ET reaction is employed, an electron may tunnel across the solution between the nanotip and the substrate to operate in the mode of scanning tunneling microscopy. Without special care,[78] it is hard to distinguish between the tunneling current and the Faradic current at the tip, thereby leaving ambiguity in the interpretation of the resultant image.[79] Accordingly, the reliable SECM imaging of a conductive substrate with a conductive tip has been limited to a spatial resolution of ~200 nm. This resolution was confirmed by quantitatively analyzing the SECM image of single Pt nanoparticles as obtained by a ~200 nm-diameter Pt tip.[42, 43]

3.2 Sturture–Permeability Relationship

The ion-selective permeability of solid-state nanoporous membranes was investigated quantitatively to confirm the structure–permeability relationship based on the effective medium theory.[80] In this theory, a membrane is perforated by an array of cylindrical nanopores to yield

$$k = 2NrD_w/(2l/\pi r\gamma + 1/f(\sigma)) \qquad (2)$$

with

$$f(\sigma) = (1+3.8\sigma^{5/4})/(1-\sigma) \qquad (3)$$

where N is the pore density, r is the pore diameter, l is the pore length, γ is the ratio of a diffusion coefficient in the pore, D_p, against a diffusion coefficient in the solution, D_s, and σ (= πNr^2) is the membrane porosity. The structure–permeability relationship is useful, for instance, to determine a pore diameter, which changes when the pore is blocked or expanded. This relationship is also useful to assess the interaction of a transported molecule with the pore, which alters the corresponding diffusion coefficient, D_p, from the solution counterpart, D_s.

The structure–permeability relationship based on eqs 2 and 3 was confirmed by measuring the permeability of an ultrathin porous membrane using a micropipet-supported ITIES as an SECM tip.[80] The high permeability of the 16 nm-thick porous membranes was measurable by using SECM owing to a high mass-transport condition between the tip and the membrane. Experimentally, an SECM tip approached the membrane vertically to obtain an approach curve, i.e., a plot of the tip current versus the tip–membrane distance. The approach curve was analyzed by the finite element simulation to determine membrane permeability. The proportionality between the membrane permeability and diffusion coefficient of various small monovalent ions was demonstrated (Fig. 5) to agree with eq 2 based on the geometrical parameters of solid nanopores i.e., r = 5.6 nm and N = 67 pores/μm^2 as determined by TEM and l = 15 nm as determined by ellipsometry. This agreement indicates that the small monovalent ions diffuse through the water-filled nanopores as freely as in the solution, i.e., $D_p = D_s$.

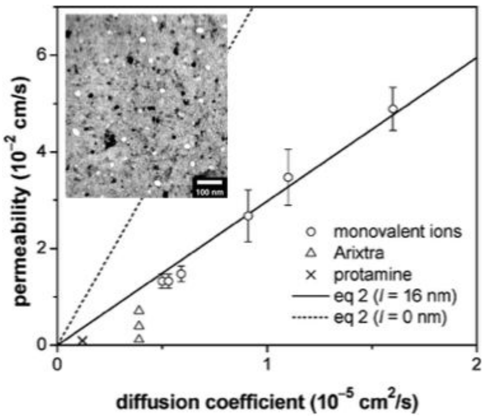

Fig. 5 Plot of the membrane permeability versus the diffusion coefficient of transported ions. The permeability to Arixtra and protamine was measured with 0.10, 0.03, and 0.01 M PBS while 0.10 M PBS was employed for monovalent ions. The inset shows a TEM image of the membrane with pores (bright circles) and diffracting nanocrystals (dark spots). Reproduced from Ref. 80 with permission from the American Chemical Society.

The structure–permeability relationship was used to reveal electrostatic and steric interactions between the pore wall and polyions. A micropipet was filled with the organic solution of an ionophore to selectively transfer a polyion, which is too hydrophilic to transfer into the organic phase without an ionophore. Specifically, dimethyldioctadecylammonium was employed as an ionophore for polyanion Arixtra,[81] a synthetic anticoagulant based on a pentasaccharide with eight sulfate and two carboxylate groups. The permeability of the nanoporous membrane to Arixtra was lower than expected from eq 2 (Fig. 5) and was lowered as the ionic strength of the solution was decreased. This result indicates that the transport of the polyanion was hindered electrostatically by the negative charge on the pore wall. The electrostatic repulsion was strengthened by decreasing the ionic strength to more weakly screen the charge of the polyanion and the pore wall. By contrast, steric hindrance was observed for protamine, a polypeptide (~4.5 kDa) with ~20 positive charges based on arginine residues. The organic phase was doped with dimetylnaphthalenesulfonate as a protamine-selective ionophore.[82] The protamine permeability of the porous membrane was lower than expected from eq 2 (Fig. 5) but was independent of the ionic strength, thereby excluding the electrostatic effect. The precise SECM measurement of the membrane permeability revealed the steric effect on protamine transport. Protamine molecules with a hydrodynamic radius of 2.0 nm were too large to freely diffuse across the nanopores with an average radius of 5.6 nm.

3.3 Nanopore-Supported ITIES Array

The structure–permeability relationship of nanoporous membranes will be useful to rationally design a highly sensitive ion sensor based on an array of the nanoscale ITIES. In principle, the sensitivity of a nano-ITIES-array sensor can be enhanced for cyclic voltammetry by decreasing the background charging current as demonstrated for an array of gold nanoelectrodes.[83] A higher sensitivity is expected for an array of smaller electrodes or interfaces as follows.[84]

When the entire macroscopic ITIES is available for an IT reaction during cyclic voltammetry, both IT current and charging current are determined geometrically by the interfacial area, A, to define a detection limit. The charging current is suppressed by blocking the interface with the insulating part of a nanoporous membrane (Fig. 6) and is determined by $A\sigma$ (= πANr^2). When pores are separated widely to support a steady-state diffusion layer at each ITIES (Fig. 6A), the resultant IT current at each pore is given by eq 1 with $a = r$ to yield the total IT current that is proportional to ANr. Accordingly, the ratio of the IT current against the background charging current is inversely proportional to the pore radius, i.e., $ANr/\pi ANr^2 = 1/\pi r$, and is enhanced proportionally by decreasing the pore size to lower the detection limit. The corresponding cyclic voltammogram becomes sigmoidal under steady states. An even lower detection limit is expected when pores are located close enough to overlap diffusion layers (Fig. 6B), where the total IT current is independent of the pore size and is determined by the total area including the insulating region, i.e., A. The corresponding ratio of the IT current against the background charging current is inversely proportional to the square of the pore radius, i.e., $A/\pi ANr^2 = 1/\pi Nr^2$. In this case, peak-shaped transient cyclic voltammograms are expected owing to the overlapping diffusion layers as demonstrated for the gold nanoelectrode array with a low nanomolar detection limit.[83]

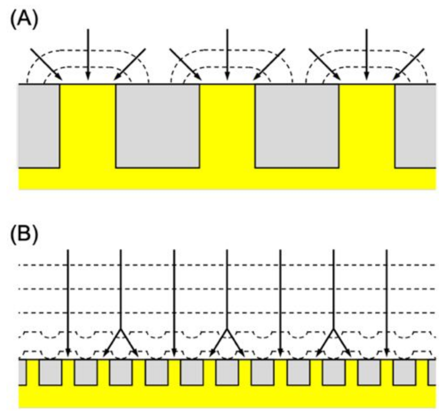

Fig. 6. Evolution of the diffusion layer at an array of nanoscale interfaces between two liquid phases (white and yellow) separated by a nanoporous membrane (gray). Arrows and dashed lines indicate the diffusional flux and the same concentrations of transferred ions, respectively. Adapted from Ref. 84 with permission from John Wiley and Sons.

Experimentally, the detection limit of nanopore-supported ITIES arrays by cyclic voltammetry has been limited to submicromolar and has not reached the low nanomolar detection limit of a gold nanoelectrode array.[83] For instance, 20 × 20 arrays of 400 pores with a radius of 17 nm were prepared with a 100-nm thick silicon nitride membrane by the combination of photo- and electron-beam lithography to detect a β-blocker drug, propranolol, with a limit of 0.8 μM.[85] The higher detection limit is attributed to the non-overlapping diffusion layer at each interface, i.e., Fig. 6A. In addition, the ITIES is more capacitive than the metal/solution interface to yield a larger charging current. More recently, an array of ~80 nm-long nanopores with diameters of 2–3 nm was prepared at a high pore density of 4×10^8 pores/μm^2 on the indium tin oxide electrode by the Stöber-solution growth approach.[86] The 80 nm-thick porous electrode was transferred to a silicon nitride membrane to support an 18 μm-diameter patch of the self-standing nanoporous membrane. The ensemble was integrated into a 3D-printed frame to develop a portable sensor for choline as the precursor and metabolite of acetylcholine and as a marker of cholinergic activity. The limit of detection, however, was only 0.99 μM.

By contrast, IT stripping voltammetry at ITIES based on solid-supported polymeric membranes can reach detection limits from nanomolar to picomolar.[5] In this case, the surface of the polymeric membrane was not covered with a porous membrane and was entirely exposed to the aqueous sample solution. An analyte ion was potentiostatically preconcentrated into a ~1 μm-thick ion-selective polymeric membrane and stripped from the thin solid-supported membrane voltammetrically and exhaustively to enhance the stripping current response. The stripping voltammetric detection limits of heparin,[87] ClO_4^-,[88] PF_6^-,[89] alkylammoniums,[89] K^+,[90] NH_4^+,[90] Ca^{2+},[91] and perfluoroalkyl sulfonates and carboxylates[92] went below the potentiometric counterpart to reach low nanomolar and low picomolar. Moreover, the voltammetric approach allows for the selective detection of multiple ions.[93-95] IT stripping voltammetry, however, requires lengthy preconcentration of an analyte for nanomolar and picomolar detection limits, which are also determined by the background charging current. A nanopore-supported ITIES array will shorten the preconcentration time of stripping voltammetry for picomolar detection limits or achieve nanomolar detection limits by cyclic voltammetry without the preconcentration step. Importantly, IT reactions are fast enough to yield well-defined diffusion-limited current responses despite the enhanced nanoscale diffusion at the partially blocked interfaces.[96, 97]

4. Nuclear Pore Complex

The nuclear pore complex (NPC) solely mediates the transport of both small molecules and macromolecules between the nucleus and cytoplasm of a eukaryotic cell to play imperative roles.[98] The NPC is crucial to the regulation of gene expression[99] and is linked to many human diseases[100] including cancers [101] and neuronal diseases.[102] The NPC represents one of the largest known protein complexes (in total ~120 MDa) and comprises multiple copies of 30 distinct proteins called nucleoporins to perforate the double-membraned nuclear envelope.[103] The selective transport barriers of the NPC are based on hydrophobic repeats of phenylalanine and glycine (FG) of nucleoporins.

The goal of this section is to introduce the biological application of ion-selective ITIES tips for SECM studies of nanoscale molecular transport through NPCs as proteinous nanopores.[104] An important takeaway is that new gating mechanisms of the NPCs, i.e., ion-induced permeabilization[105] and electrostatic gating,[106] were discovered in these SECM studies. These findings were made by investigating the NPC-mediated transport of redox-inactive ions[105] including polyions[106] with microscale ITIES tips. Previously, Pt UMEs were employed as microscale SECM tips to establish the non-destructive and non-contact measurement of the high NPC permeability to various redox-active ions.[107-109] These studies employed the large nucleus isolated from the oocyte of *Xenopus laevis* to enable SECM of the nuclear envelope at the intact nucleus[107, 108] or spread over the microporous membrane.[109] Significantly, nanopipet-supported ITIES tips are more robust than solid nanotips (Fig. 1) and are promising for future SECM imaging of single NPCs (Fig. 4).

4.1 Ion Permeability and Ion-Induced Permeabilization

The structure–permeability relationship of the NPC was investigated by employing small monovalent ions as SECM probes to find that the NPC nanopore is permeabilized by highly hydrophobic ions.[105] The hydrophobicity of the examined ions was determined by cyclic voltammetry at micropipet-supported ITIES. A more hydrophobic cation was transferred into the inner organic phase at more positive potentials. The resultant order of ion hydrophobicity was tetraphenylarsonium (TPhAs$^+$) > TBA$^+$ > (ferrocenylmethyl)trimethyl ammonium (FcTMA$^+$). By contrast, the transfer of a more hydrophobic anion required more negative potential to follow the order of perfluorobutylsulfonate[110] (PFBS$^-$) > PF$_6^-$ > ClO$_4^-$. The permeability of the NPCs to these ions was measured at the nuclear envelope of the intact nucleus by using micropipet-supported ITIES as SECM tips (Fig. 7) to vary with the diffusion coefficient of the transported ions in the aqueous solution as expected from eq 2. The slope was consistent with N = 40 NPCs/μm^2, r = 24 nm, and l = 35 nm as determined for the NPC of the *Xenopus* oocyte nucleus by cryogenic TEM and ambient AFM. This result indicates that these small ions diffuse through the transport barriers of the NPC as freely as in the aqueous solution, i.e., $D_p = D_s$ in eq 2. These ions are smaller than the size of water-filled spaces (5.2 nm) among the gel-like network of FG repeats in the transport barriers.[111]

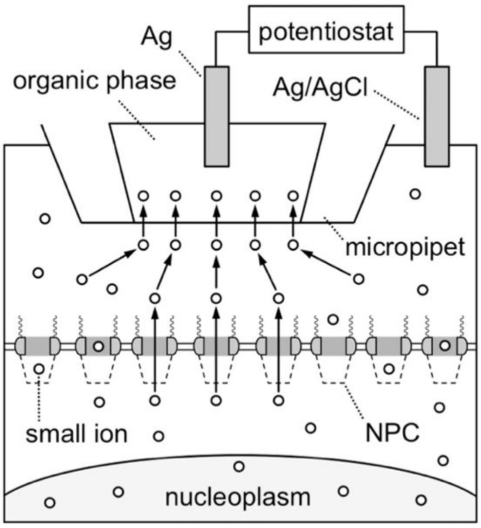

Fig. 7 SECM permeability measurement of the NPCs using a micropipet-supported ITIES tip. The nucleus was swollen to detach the nuclear envelope from the nucleoplasm. Reproduced from Ref. 105 with permission from the American Chemical Society.

Interactions between FG-rich transport barriers and small hydrophobic ions, i.e., TPhAs$^+$ and PFBS$^-$, were strong enough to permeabilize the NPC to passively impermeable albumin. The NPC was permeabilized when the intact nucleus was immersed in the solution containing a high concentration of the hydrophobic ions. The permeabilized NPC became impermeable to albumin when the hydrophobic ions were removed from the bathing solution. The reversible permeabilization of the transport barriers by the hydrophobic ions contrasts with the irreversible permeabilization by other chemicals such as hydrophobic alcohols.[112] Interestingly, the ion-permeabilized NPC was not permeable to albumin in the presence of wheat germ agglutinin (WGA), which binds the nucleoporins at the periphery of the NPC nanopore.[113] This result indicates that the hydrophobic ions permeabilized the peripheral route of the NPC. Moreover, the transport of the importin–albumin complex was blocked by WGA in the absence of the hydrophobic ions, but not in their presence. This result indicates that the hydrophobic ions permeabilized the central route of the NPC to the importin–albumin complex, which is naturally transported through the peripheral route. These unexpected findings were made by the study of non-natural ions to support that the interior of the NPC nanopore is heterogeneously organized into central and peripheral routes.[108]

It should be noted that the water-immiscible organic solvent of the pipet-supported ITIES is significantly soluble in water. In the SECM studies of NPCs, the same permeability to FcTMA$^+$ was obtained by using both Pt[108] and ITIES[105] tips. This result validates that the organic solvent leached from the latter did not alter the permeability of the NPCs under the tip. More recently, extremely hydrophobic organic solvents were examined to replace readily leachable organic solvents for biological studies.[114, 115] Without these cautions, the application of ITIES tips to the study of contamination-sensitive systems, e.g., solid electrocatalysts,[116] may cause an unnoticed artifact.[117]

4.2 Nanoscale Electrostatic Gating

Nucleoporins possess various populations of hydrophobic and charged amino acids to sort out different macromolecules into different pathways not exclusively by hydrophobic interactions, but cooperatively with electrostatic interactions. This hypothesis was made theoretically[118, 119] and confirmed experimentally by employing micropipet-supported ITIES as polyion-selective SECM tips.[106] In this experimental work, the nuclear envelope of the *Xenopus* oocyte nucleus was detached from the nucleoplasm, which leaches small passively permeable proteins to foul the SECM tips. The nucleoplasm-free nuclear envelope was supported by microporous membranes[109] to investigate the patch of the nuclear envelope by SECM. Experimentally, the micropore-supported patch of the nuclear envelope was located by SECM imaging. The SECM tip approached the center of the nuclear envelope patch while measuring the tip current, thereby obtaining an approach curve as analyzed by the finite element method (Fig. 8A). The tip current decreased gradually as the tip approached the nuclear envelope, which was only partially permeable to protamines. The tip current, however, was much higher than expected at an impermeable substrate, e.g., SiO_2 in Fig. 8, because the NPC was permeable to protamine with a molecular weight of only 4.5 kDa. The tip current based on protamine transfer at the micropipet-supported ITIES tip became lower as the ionic strength of the solution was lowered. This result indicates that the passive transport of protamine through the NPC was electrostatically hindered by positively charged residues of transport barriers. Moreover, the permeability of the NPC to protamine was not lowered by the addition of WGA, which blocks the peripheral route. This result indicates that protamine transport was electrostatically prevented through the peripheral route and was only mediated through the central route. By contrast, no effect of ionic strength was observed for polyanion Arixtra to indicate negligible electrostatic effects from anionic residues, which are less abundant than cationic residues.

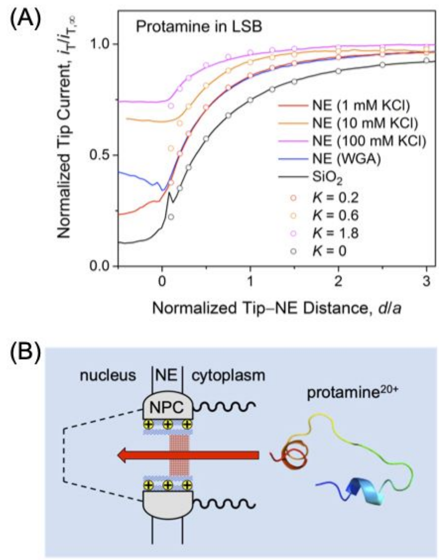

Fig. 8 (A) Experimental (lines) and simulated (circles) approach curves of protamine at the micropore-supported nuclear envelope in the low salt buffer (LSB) at pH 7. The tip inner and outer radii are 1.5 and 2.2 μm, respectively. (B) Scheme of protamine transport through the central route of the NPC with the electrostatically blocked peripheral route. Reproduced from Ref. 106 with permission from the Royal Society of Chemistry.

The permeability of the NPC to protamine was analyzed by using the structure–permeability relationship established for small ions at both intact nuclei and micropore-supported nuclear envelopes (eq 2). When the ionic strength of the solution was sufficiently high, the permeability of the NPC to protamine agreed with that of small ions. This result indicates that protamine diffuses through the NPC barrier as freely as in the aqueous solution. The hydrodynamic diameter of protamine (4.0 nm) is smaller than the size of water-filled spaces (5.2 nm) among the gel-like network of FG repeats in the transport barriers.[111] As the ionic strength was lowered, the corresponding Debye length increased to electrostatically block the passive transport of protamine. The resultant protamine permeability of the NPC corresponded to a smaller pore diameter of 20.8 nm in eq 2 when other parameters remained the same. This result indicates that a 13.6 nm-thick peripheral region of a 48 nm-diameter pore was electrostatically blocked against protamine transport (Fig. 8B). We attributed the electrostatic effect to a peripheral nucleoporin, POM121, which has a high population of cationic residues in comparison with anionic residues and even FG dipeptides. Interestingly, the functional role of cationic residues contrasts with the structural role of anionic residues, which maintain the spatial distribution of FG domains.[106, 120]

5. Bacteria

In this section, we aim at discussing how the capability to electrochemically detect redox-inactive ions at liquid/liquid interfaces can be useful for studies of bacterial physiology. A major takeaway is that the in-situ and real-time detection of redox-inactive bacterial metabolites (CO_3^{2-}[27] and lactate[26]) was enabled recently by employing nanopipet-supported ITIES tips. The combination of SECM with nanopipet-supported ITIES tips allowed for the study of a small number of bacteria[27] and even for the imaging of a single bacterium.[26] Nanopipet-supported ITIES tips can be also useful for the detection of antibacterial drugs,[33] which are often redox-inactive. Previously, SECM based on redox-active solid microtips was employed to spatially resolve bacterial biofilms and aggregates, which revealed new information about bacterial physiology. Specifically, a 25 µm-diameter gold tip was used to detect hydrogen peroxide produced by the fermentation of sugars into lactic acid in the biofilms of oral bacteria, *Streptococcus gordonii*.[121] Moreover, a 10 µm-diameter Pt tip was employed to discover the “electrocline” of pyocyanin (PYO) released from the biofilm of a pathogenic Gram-negative bacterium, *Pseudomonas aeruginosa*.[122] Most recently, the 3D-microprinting technology was combined with microscale SECM[123] to successfully study PYO-based quorum sensing in and among aggregates containing a well-controlled number of *Pseudomonas aeruginosa* cells.[124]

5.1. Uptake of Antimicrobial Ag^+

The application of electrochemistry at liquid/liquid interfaces to studies of bacterial physiology was demonstrated by Bard and co-workers.[125] In this work, a micropipet-supported ITIES tip was doped with Ag^+-selective ionophore IV for differential pulse voltammetry of Ag^+. A Pt tip was used in an earlier study to detect Ag^+ by stripping voltammetry.[126] SECM measurements with a Ag^+-selective ITIES tip revealed that the uptake of antimicrobial Ag^+ by *Escherichia coli* (*E. coli*) was enhanced in the presence of 4-aminopyridine (4-AP), a blocker of potassium channels. Specifically, *E. coli* was implanted in a collagen gel (Fig. 9) at a concentration of ~10^{11} colony-forming units. A Ag^+-selective micropipet tip was positioned above the collagen gel to monitor a time-dependent change in Ag^+ concentration in the droplet. With a higher concentration of 4-AP, the Ag^+ concentration dropped more quickly to reach a lower steady value. This result indicates that 4-AP promotes not only the uptake rate but also the amount of Ag^+ taken up by *E. coli*. The time profile was analyzed quantitatively to yield 1.5×10^4, 3.5×10^4, and 5.9×10^4 ions per cell per sec for 0.1 mM Ag_2SO_4, with 0, 0.5, and 1 mM 4-AP, respectively. In addition, a Hg-covered Pt tip was employed as an O_2 microsensor to find that the respiration rate of the *E. coli* cells also decreased with an increase in the 4-AP concentration. A respiratory activity, however, was maintained with 1 mM 4-AP to confirm the viability of *E. coli*.

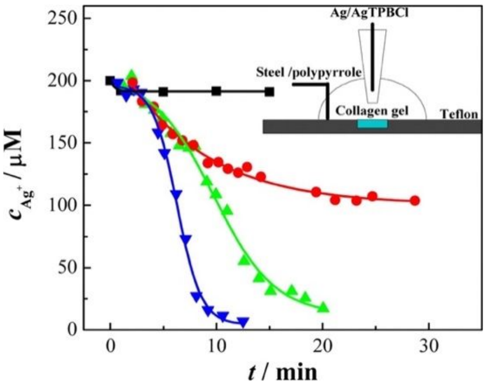

Fig. 9 Ag^+ concentration near a collagen gel (black squares) without *E. coli* exposed to 0.1 mM Ag_2SO_4, or with *E. coli* exposed to (red circles) 0.1 mM Ag_2SO_4, (green triangles) 0.1 mM Ag_2SO_4 and 0.5 mM 4-AP, or (blue inverted triangles) 0.1 mM Ag_2SO_4 and 1 mM 4-AP. The inset shows a schematic for the SECM detection of Ag^+ in the bulk droplet. Reproduced from Ref. 125. Copyright 2008 National Academy of Sciences.

5.2. Metabolic CO_3^{2-} Production

CO_3^{2-} is an important metabolite and a reactant or product in reactions relevant to sustainable energy and environmental applications. Specifically, CO_3^{2-} is a metabolic product of microbial fuel oxidation and a reactant for microbial electrosynthesis.[127, 128] Accordingly, the direct sensing of local concentration of CO_3^{2-} with high sensitivity is required to profoundly elucidate the given systems. Amperometric sensing is more affordable for high sensitivity due to the direct dependence of current on the concentration, while potentiometric sensing logarithmically depends on the concentration.[129] Moreover, CO_3^{2-} sensing with nanoscale probes allows for a study at a high spatial resolution, thereby scrutinizing individual levels of bacteria and establishing the structure–reactivity relationship.

We developed nanoscale CO_3^{2-}-selective amperometric/voltammetric probes using a nanopipet-supported ITIES (Fig. 10A).[27] The recognition of CO_3^{2-} was mediated by highly selective molecular-tweezer-type CO_3^{2-} ionophore VII via covalent bond formation.[130] The fundamental understanding to realize this nanoscale CO_3^{2-} probe was newly addressed through both theoretical and experimental studies. These studies assessed the slow dissolution and pre-activation of the ionophore in the organic phase, a peculiar solubility at the nanoscale interface, and the cleanness of the nanoscale ITIES. Highly reproducible and reliable nanopipet voltammograms could be obtained for ionophore-facilitated CO_3^{2-} transfer (Fig. 10B), which enabled us to mechanistically and kinetically evaluate the given IT reaction. The one-step mechanism of the electrochemical interfacial CO_3^{2-} transfer concerted by ionophore complexation (E mechanism) is a plausible mechanism with the standard rate constant of $k^0 = 0.048$ cm/s. This k^0 value is similar to reported values for Ag^+, K^+, and Ba^{2+} with non-covalent-bonding ionophores,[131] implying a weak covalent bond formation between CO_3^{2-} and the ionophore. By contrast, the two-step mechanism of the electrochemical IT reaction followed by the chemical complexation reaction (EC mechanism) could be excluded. A good fit of experimental voltammograms with the EC mechanism required the unrealistically high standard rate constant of CO_3^{2-} transfer as well as the large association constant between CO_3^{2-} and ionophore VII exceeding a diffusion limit.

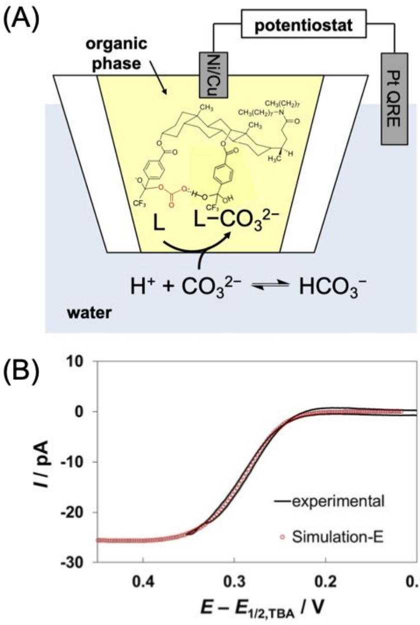

Fig. 10 (A) Scheme and (B) steady-state voltammogram of CO_3^{2-} transfer across the 1,2-dichloroethane/water interface supported by the nanopipet filled with a *premade* 30 mM ionophore solution. The best theoretical fitting (red open circles) to the experimental curves (black solid curves, background subtracted forward wave) was calculated for the E mechanism from simulations with COMSOL Multiphysics. Reproduced from Ref. 27 with permission from the American Chemical Society.

The analytical utility of the amperometric CO_3^{2-}-selective nanopipet was validated by directly measuring CO_3^{2-} produced by the ensemble of metal-reducing bacteria, *Shewanella oneidensis*, through microbial fuel oxidation. The CO_3^{2-} concentrations of 0.70 ± 0.04 mM were estimated from pristine voltammograms and confirmed by the standard addition method with 0.67 ± 0.03 mM. The electrochemically measured CO_3^{2-} concentrations were similar to the total dissolved inorganic carbon of 0.2 mM including CO_2, HCO_3^-, and CO_3^{2-} as reported for another *Shewanella* strain.[132] Now, we envision that this amperometric CO_3^{2-} nanoprobe can be employed as an SECM tip to investigate extracellular electron transport through metal-reducing bacteria at a single cell level.[26]

5.3. Nanoelectrochemical Antibiotics Sensing

Direct probing of pristine drug molecules is crucial to quantitatively assess their permeation through bacteria membranes, thus elucidating bacterial drug resistance. Liquid/liquid interfaces have been used as probes to sense pristine drug molecules via interfacial IT with voltammetric techniques.[133] IT voltammetry at the ITIES is advantageous to detect many antibiotics, which undergo acid-base equilibria without redox activity and form either cation or anion at the physiological pH. Moreover, the liquid/liquid interfaces can be utilized instead of biological membranes to obtain the physicochemical property of drugs.[134] Accordingly, the kinetic study of interfacial drug-ion transfer can offer information about the drug permeability across the artificial membrane, and provide a clue of drug structure and permeability relationship.

We applied cyclic voltammetry with nanopipet-supported ITIES to study antibiotic quinolones and sulfonamide derivatives (Fig. 11).[33] Well-defined voltammograms of the hydrophobic ions were obtained without an ionophore to reliably determine the permeability of each drug ion. Surprisingly, lipophilic drugs containing aromatic rings feature c.a. 3 order of magnitude slower rates of interfacial IT, i.e., lower permeability than small hydrophobic cation, TBA^+. This slower drug-ion transfer could be attributed to the strong interaction between water fingers and localized charges on carboxylate or amide group of drug-ions at the liquid/liquid interface.[135, 136] The relative hydrophobicity of drugs compared to the small hydrophobic anion, ClO_4^-, could be estimated during interfacial IT by comparing their $E_{1/2}$ values in the resulting voltammograms, which revealed that drugs are 2–6 orders of magnitude more hydrophilic than ClO_4^-.[33] The high hydrophilicity of drug ions is consistent with the slow IT kinetics, i.e., low permeability as determined by nanopipet voltammetry. Hereby, voltammetry with a nanopipet-supported ITIES could provide a useful tool to fundamentally study the physicochemical properties of pristine drugs, e.g., permeability and relative hydrophobicity (or apparent-hydrophilicity), thus suggesting insight into the relationship between the drug structure and permeability. We envision that a nanopipet-supported ITIES tip can be employed for SECM to real-time investigate the permeability of pristine drugs through a real bacterial membrane at a single living bacterium.[26] Such an SECM study will enable us to elucidate the relation of bacterial drug resistance with the inherent permeability and structure of drugs.

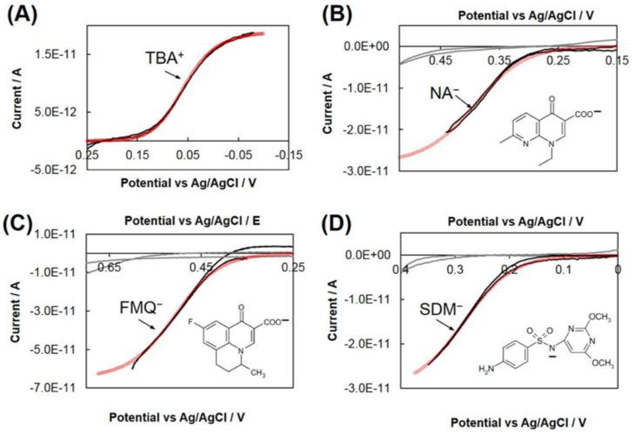

Fig. 11 Steady-state voltammograms of (A) TBA^+, (B) NA^-, (C) FMQ^-, (D) SDM^- transfers across nanopipet-supported 1,2-dichloroethane/water interfaces. The scan rate is 25 mV/s. The best theoretical fitting (red open circles) to the experimental curves (black solid curves) was calculated from simulations with COMSOL Multiphysics. Voltammograms of blank buffer solutions (gray solid curves) are plotted for NA (nalidixic acid), FMQ (flumequine), and SDM (sulfadimethoxine). Reproduced from Ref. 33 with permission from the American Chemical Society.

6. Advanced NEs

Finally, we aim at introducing our fundamental studies focused on the development and characterization of advanced NEs toward the analytical application of single-entity electrochemistry.[137-139] A major takeaway is that the electrochemical measurement of single NEs allowed us to optimize the composition of the NEs for the highly sensitive detection of an aromatic toxicant at the low nanomolar level. Specifically, the NEs were prepared from a triblock copolymer, Pluronic F-127, with the central hydrophobic chain of poly(propylene oxide) flanked by two hydrophilic chains of poly(ethylene glycol). The biocompatible NEs were applied for fluorescence imaging of intracellular oxygen and pH.[140] In addition, we introduce the recent discovery of ionosomes as a new form of NEs as probed by employing the micropipet-supported liquid/liquid interface.[64-66] Uniquely, ionosomes are stabilized not by surfactants but by ion pairs formed across the interface.

6.1. Electron Transfer

The application of biocompatible NEs to electroanalysis relies on how efficiently electron transfer occurs across the NE/electrode interface. We uniquely applied single-entity electrochemistry to investigate the interfacial structure and relevant electrochemical activity of NEs.[137] Specifically, the highly monodisperse NEs with ~40 nm diameter were composed of biocompatible surfactants of Pluronic F-127, castor oil as plasticizers, and ion exchangers e.g., potassium tetrakis(pentafluorophenyl)borate. The ensemble measurements by dynamic light scattering with two types of NEs, i.e., NE85 and NE250 in Fig. 12A, having distinctly different ratios of surfactant to oil exhibited similar sizes. These NEs, however, had dramatically different ζ-potentials as a measure of surface charges of NEs, thereby implying different interfacial structures of NEs. We hypothesized that the uneven distribution of tetrakis(pentafluorophenyl)borate inside NEs with a low fraction of surfactants (i.e., NE85) forms a borate inner layer for additional structural stabilization, thus affecting the interfacial structure of NEs (Fig. 12A left), while borates are randomly dispersed inside NEs with the high fraction of surfactant (i.e., NE250, Fig. 12A right). This structural hypothesis was proved by single-entity electrochemistry. ET reactions occurring at an individual NE containing ferrocene (Fc) were selectively monitored upon each collision of NEs onto a Pt UME under a sufficient anodic potential. NEs with a high fraction of surfactants (NE250) showed the characteristically sharp current-spike response due to the rapid oxidation of Fc upon the collision (Fig. 12B). A current response was not observed with NE85, where the borate inner layer could slow down ET across the NE/UME interface by acting as a tunneling barrier.[141] The Pt UME potential was increased to overcome a tunneling barrier and accelerate the electron transfer to drive Fc oxidation inside a NE. Resultantly, a series of current-spike responses could be obtained with NE85 during the single-entity electrochemistry. This result confirms not only the presence of the borate inner layer at the NE interface but also its electrochemical property as a tunneling barrier. Overall, the unique electrochemical approach with the single-entity electrochemistry enabled us to elucidate the relation between structures and the electrochemical functionality of NEs. This study also provided quantitative criteria for the proper composition of NEs regarding their activity in electrochemical applications.

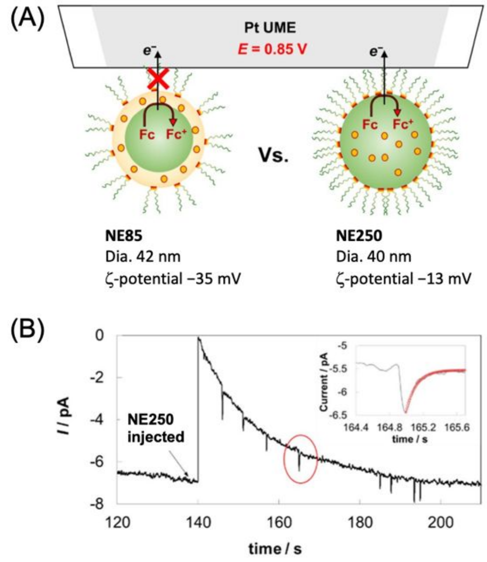

Fig. 12 (A) Schematic illustrations of hypothesized structures of NE85 (left) and NE250 (right). NE85 has a borate inner layer, while NE250 has randomly distributed borates (not to scale). (B) *I*–*t* curve of NE250 collisions at Pt UME under 0.85 V vs Pt quasi-reference electrode. 8 pM of NEs containing ferrocene (Fc) was added to the aqueous bulk solution. Each current spike corresponds to the individual collisions of NEs onto a Pt UME. Reproduced from Ref. 137 with permission from the American Chemical Society.

6.2. Molecular Transport

Molecular transport through NE/solution interfaces can be practically applied to the ultra-trace level analysis, where NEs are utilized as nanoextractors to separate and preconcentrate hydrophobic analytes from aqueous bulk media and are *in situ* electrochemically sensed by the single-entity electrochemistry (Fig. 13A).[138, 139] Pluronic F-127 functionalized NEs were employed to extract and preconcentrate target analytes, e.g., ferrocenemethanol and 2-aminobiphenyl (2-ABP) as a model of ubiquitous aromatic-toxicants dissolved in water. The *in situ* detection and quantitative estimate of analytes extracted in individual NEs were made via the oxidation of extracted analytes upon a NE collision onto a Pt UME. Extraction was markedly efficient to reach ~8 orders of magnitude of preconcentration factor under the true equilibrium.[138, 139] The resultant ultra-trace level analysis reached a detection limit of ~0.2 ppb for ferrocenemethanol and ~0.1 ppb for 2-ABP. Notably, sigmoidal calibration curves were constructed for quantitative analysis by performing a series of single-entity electrochemistry with varying concentrations of NEs and analytes in the aqueous bulk solution (Fig. 13B).[138] The charge densities estimated at individual NEs were plotted as a function of the total concentration of analytes added to the solution. Sub-ppb detection limits were obtained by modulating the concentration of NEs in the bulk solution, thereby controlling the number of analytes extracted in each NE. Given the excellent detection performance as well as the broad applicability, the introduction of selectivity factors in NEs such as ionophores or chelators for specific analytes is envisioned. The combination of selective NEs with single-entity electrochemistry will offer great prospects as a sensor for environmental and bioanalytical applications.

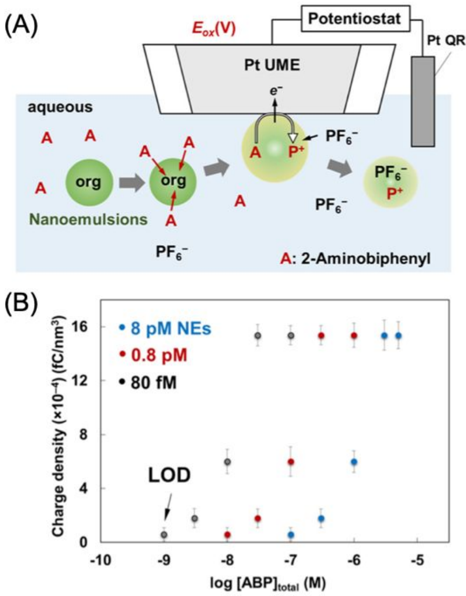

Fig. 13 (A) A schematic illustration of single-entity electrochemical measurements using NEs as nanoextractors to effectively scavenge target compounds, A, from water to NEs, and electrochemically sense them by oxidation (or, reduction) upon the collision of NE. Reproduced from Ref. 124 with permission from the American Chemical Society. (B) Charge density curves vs. logarithm of 2-ABP concentration in aqueous bulk solution in the presence of 8 pM (blue circles), 0.8 pM (red circles), and 80 fM NEs (grey circles), respectively. Reproduced from Ref. 138 with permission from Elsevier.

6.3. Ionosome

A micropipet-supported liquid/liquid interface was employed to form and detect a new type of NE, ionosome, which is based on a water droplet stabilized by a pair of aqueous and organic electrolytes.[64] The formation of ionosome was initiated by the transfer of a highly hydrophilic ion, e.g., Li^+ (Fig. 14) or $Cl^–$, from the aqueous phase into the organic phase. Water molecules were drugged and surrounded by the transferred ions, which were stabilized by organic counterions, i.e., tetrakis(pentafluorophenyl)borate or bis(triphenyl-phosphoranylidene)ammonium, respectively. When the interfacial potential was reversed, the collision of single ionosomes at the interface resulted in the release of the transferred ions into the aqueous phase to yield current spikes. The polarity of the spike current depended on the charge of the transferred ions. Ionosome sizes were determined from the charge associated with the spike currents by assuming that the transferred ions were closely packed on the spherical surface of the ionosomes. The electrochemically estimated diameter of 150–170 nm agreed well with the diameter of 120 nm as estimated by dynamic light scattering. Ionosomes were considered nanometer-sized capacitors that store energy in the electrical double layer formed between hydrated ions at the aqueous side and hydrophobic counterions at the organic side. Recent studies also demonstrated that the fusion of ionosomes at the liquid/liquid interface followed the bulk electrolysis model[61] as represented by an exponential decay of the spike current.[65, 66]

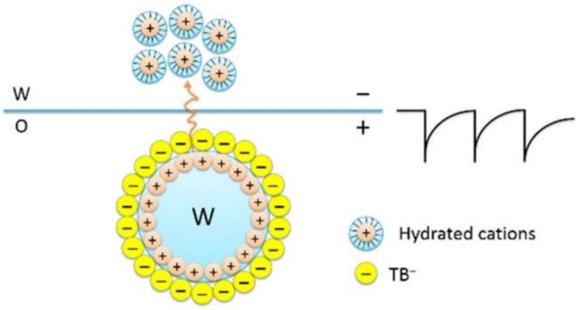

Fig. 14 Schematic diagram of the electrochemical in situ generation and detection of single ionosomes based on the transfer of hydrated cations at the ITIES formed at the tip of an aqueous-electrolyte-filled micropipet in an immiscible organic solution with bis(triphenylphosphoranylidene)ammonium tetrakis(pentafluorophenyl)borate, $BA^+TB^–$, as the supporting electrolyte. A constant positive bias is applied to drive the transfer of the hydrated cations from "w" in the pipet into the "o" phase for ionosome formation. Soon afterward, the bias is reversed to observe negative ionic current spikes based on the fusion of the ionosomes on the oil side of the ITIES for the release of the hydrated cations. Reproduced from Ref. 64 with permission from the American Chemical Society.

7. Challenges and Opportunities

Remarkable progress has been made in the development and application of nanoelectroanalytical methods based on liquid/liquid interfaces. There, however, are still a lot of room for the future advancement of the already powerful methods in selectivity and sensitivity.

High selectivity is required for a wider range of applications to detect target ions in complex samples. For instance, the highly selective ionophores developed for potentiometry[142] were successfully applied to amperometry/voltammetry at the microscale ITIES[125, 131, 143] to enable the nanoscale counterpart only recently.[27] This nanotechnological breakthrough will allow for the utilization of not only commercially available ionophores but also the ionophores that have been developed in the field of supramolecular chemistry. In comparison with equilibrium potentiometry, the highly selective detection of multiple ions is achieved by dynamic voltammetry based on both thermodynamics and kinetics of ionophore-facilitated/accelerated IT reactions.[93-95] The fast nanoscale IT reaction facilitated by a highly selective ionophore[27] is promising for the development of the ion sensor based on an array of the nanoscale ITIES. The incorporation of ionophores into NEs is also feasible[144] and attractive for sensing applications of single-entity electrochemistry. Moreover, the voltammetric characterization of newly synthesized ionophores will be informative to gain both thermodynamic and kinetic insights into the ionophore–ion recognition mechanism at the ITIES.[27, 131] The voltammetric information will be especially useful for the advancement of anion recognition, which is more challenging and less established than cation recognition.[145] The selective recognition of an anionic group, e.g., carboxylate,[146] will widen the applicability of nanoelectrochemistry at liquid/liquid interfaces for various applications. For instance, neurotransmitters with a carboxylate group, e.g., gamma-aminobutyric acid and glutamate, are redox-inactive and can be zwitterions, which are detectable electrochemically by using the ITIES.[147, 148]

A high sensitivity will enable us not only to detect lower concentrations of target ions but also to improve spatial and temporal resolutions. A higher spatial resolution requires a smaller nanopipet or a smaller NE to sample a local concentration of a target ion in a smaller volume. A smaller nanopipet will also improve the spatial resolution of SECM imaging. Advantageously, the amperometric response of a nanoscale SECM tip is less affected by convection to reach a steady state more quickly, thereby enabling faster imaging with higher temporal resolution.[78] Moreover, faster SECM imaging allows us to implement a more advanced algorithm than the standard constant-height imaging, thereby simultaneously resolving the topography and reactivity of a complex substrate.[149] Currently, the smallest size of a nanopipet is limited to ~10 nm by the capability of the laser-based pipet puller. The diameter of NEs studied by single-entity electrochemistry is usually larger than 100 nm but can be as small as 40 nm.[137-139] Experimentally, either a smaller nanopipet or a smaller NE requires the measurement of lower current, which is eventually limited by the shot noise to ~2,000 electrons for a given temporal resolution.[150] This limitation was discussed in the recent study of K^+ transport by single valinomycin molecules through the bilayer lipid membrane.[151]

Conflicts of interest

There are no conflicts to declare.

Acknowledgements

This work was supported by the National Science Foundation with a CAREER award (CHE-2046363) for JK and the National Institutes of Health (R01GM112656) for SA.

References

1. H. H. Girault and D. J. Schiffrin, Electrochemistry of Liquid-Liquid Interfaces in *Electroanalytical Chemistry*, ed. A. J. Bard, Marcel Dekker, New York, 1989, vol. 15, pp. 1–141.
2. H. H. Girault, Electrochemistry at Liquid-Liquid Interfaces in *Electroanalytical Chemistry*, eds. A. J. Bard and C. G. Zoski, Taylor & Francis, Boca Raton, 2010, vol. 23, pp. 1–104.
3. Z. Samec, *Pure Appl. Chem.*, 2004, **76**, 2147–2180.
4. S. Amemiya, Potentiometric Ion-Selective Electrodes in *Handbook of Electrochemistry*, ed. C. G. Zoski, Elsevier, New York, 2007, pp. 261–294.
5. S. Amemiya, J. Kim, A. Izadyar, B. Kabagambe, M. Shen and R. Ishimatsu, *Electrochim. Acta*, 2013, **110**, 836–845.
6. R. A. Marcus, *J. Chem. Phys.*, 2000, **113**, 1618–1629.
7. R. A. Marcus, *J. Phys. Chem.*, 1990, **94**, 4152–4155.
8. R. A. Marcus, *J. Phys. Chem.*, 1991, **94**, 2010–2013.
9. I. Benjamin, *Science*, 1993, **261**, 1558.
10. Y. Wang, J. Velmurugan, M. V. Mirkin, P. J. Rodgers, J. Kim and S. Amemiya, *Anal. Chem.*, 2010, **82**, 77–83.
11. P. J. Rodgers, S. Amemiya, Y. Wang and M. V. Mirkin, *Anal. Chem.*, 2010, **82**, 84–90.
12. R. A. Marcus, *J. Chem. Phys.*, 1965, **43**, 679–701.
13. A. L. Barker, P. R. Unwin, S. Amemiya, J. F. Zhou and A. J. Bard, *J. Phys. Chem. B*, 1999, **103**, 7260–7269.
14. S. J. Liu, Q. Li and Y. H. Shao, *Chem. Soc. Rev.*, 2011, **40**, 2236–2253.
15. S. Amemiya, Y. Wang and M. V. Mirkin, Nanoelectrochemistry at Liquid/Liquid Interfaces in *Specialist Periodical Reports in Electrochemistry*, eds. R. G. Compton and J. D. Wadhawan, RSC, 2013, vol. 12, pp. 1–43.
16. S. Voci and J. E. Dick, *Curr. Opin. Electrochem.*, 2023, **39**, 101244.
17. E. Laborda and A. Molina, *Curr. Opin. Electrochem.*, 2021, **26**, 100664.
18. L. A. Baker, *J. Am. Chem. Soc.*, 2018, **140**, 15549–15559.
19. A. J. Bard, L. R. Faulkner and H. S. White, *Electrochemical Methods: Fundamentals and Applications*, John Wiley & Sons, New York, 3rd edn., 2022, p. 851.
20. C. B. Milton, K. Xu and M. Shen, *Curr. Opin. Electrochem.*, 2022, **34**, 101005.
21. H. D. Jetmore, E. S. Anupriya, T. J. Cress and M. Shen, *Anal. Chem.*, 2022, **94**, 16519–16527.
22. A. Gamero-Quijano, G. Herzog, P. Peljo and M. D. Scanlon, *Curr. Opin. Electrochem.*, 2023, **38**, 101212.
23. S. Amemiya, Scanning Electrochemical Microscopy of Nanopores, Nanocarbons, and Nanoparticles in *Nanoelectrochemistry*, eds. M. V. Mirkin and S. Amemiya, Taylor and Francis, Boca Raton, FL, 2015, pp. 621–653.
24. S. Amemiya, Nanoscale Scanning Electrochemical Microscopy in *Electroanalytical Chemistry*, eds. A. J. Bard and C. G. Zoski, CRC Press, 2015, pp. 1–72.
25. M. L. Colombo, J. V. Sweedler and M. Shen, *Anal. Chem.*, 2015, **87**, 5095–5100.
26. S. R. Puri, E. Almeida, S. Elangovan, A. Labossiere, C. Collins, M. Ramsey and J. Kim, *Anal. Chem.*, 2023, **95**, 8711–8719.
27. S. Elangovan, S. R. Puri, H. Madawala, J. Pantano, B. Pellock, M. K. Kiesewetter and J. Kim, *Anal. Chem.*, 2023, **95**, 4271–4281.
28. M. Shen, Z. Qu, J. DesLaurier, T. M. Welle, J. V. Sweedler and R. Chen, *J. Am. Chem. Soc.*, 2018, **140**, 7764–7768.
29. Theresa M. Welle, K. Alanis, M. L. Colombo, J. V. Sweedler and M. Shen, *Chem. Sci.*, 2018, **9**, 4937–4941.
30. X. Y. Zhu, Y. H. Qiao, X. Zhang, S. S. Zhang, X. H. Yin, J. Gu, Y. Chen, Z. W. Zhu, M. X. Li and Y. H. Shao, *Anal. Chem.*, 2014, **86**, 7001–7008.
31. C. Lefrou, *J. Electroanal. Chem.*, 2006, **592**, 103–112.
32. P. J. Rodgers and S. Amemiya, *Anal. Chem.*, 2007, **79**, 9276–9285.
33. S. R. Puri and J. Kim, *Anal. Chem.*, 2019, **91**, 1873–1879.
34. R. Chen, R. J. Balla, A. Lima and S. Amemiya, *Anal. Chem.*, 2017, **89**, 9946–9952.
35. N. Nioradze, R. Chen, J. Kim, M. Shen, P. Santhosh and S. Amemiya, *Anal. Chem.*, 2013, **85**, 6198–6202.
36. R. Chen, K. Hu, Y. Yu, M. V. Mirkin and S. Amemiya, *J. Electrochem. Soc.*, 2016, **163**, H3032–H3037.
37. K. Shigyou, L. Sun, R. Yajima, S. Takigaura, M. Tajima, H. Furusho, Y. Kikuchi, K. Miyazawa, T. Fukuma, A. Taoka, T. Ando and S. Watanabe, *Anal. Chem.*, 2020, **92**, 15388–15393.
38. E. S. Anupriya and M. Shen, *J. Electrochem. Soc.*, 2022, **169**, 046501.
39. M. Shen, R. Ishimatsu, J. Kim and S. Amemiya, *J. Am. Chem. Soc.*, 2012, **134**, 9856–9859.
40. R. M. Penner, M. J. Heben, T. L. Longin and N. S. Lewis, *Science*, 1990, **250**, 1118–1121.

41. W. L. Underkofler and I. Shain, *Anal. Chem.*, 1963, **35**, 1778–1783.
42. J. Kim, C. Renault, N. Nioradze, N. Arroyo-Currás, K. C. Leonard and A. J. Bard, *Anal. Chem.*, 2016, **88**, 10284–10289.
43. J. Kim, C. Renault, N. Nioradze, N. Arroyo-Currás, K. C. Leonard and A. J. Bard, *J. Am. Chem. Soc.*, 2016, **138**, 8560–8568.
44. S. Amemiya, R. Chen, N. Nioradze and J. Kim, *Acc. Chem. Res.*, 2016, **49**, 2007–2014.
45. J. Kim, M. Shen, N. Nioradze and S. Amemiya, *Anal. Chem.*, 2012, **84**, 3489–3492.
46. R. Chen, N. Nioradze, P. Santhosh, Z. Li, S. P. Surwade, G. J. Shenoy, D. G. Parobek, M. A. Kim, H. Liu and S. Amemiya, *Angew. Chem. Int. Ed.*, 2015, **54**, 15134–15137.
47. N. Nioradze, R. Chen, N. Kurapati, A. Khvataeva-Domanov, S. Mabic and S. Amemiya, *Anal. Chem.*, 2015, **87**, 4836–4843.
48. R. Chen, R. J. Balla, Z. T. Li, H. T. Liu and S. Amemiya, *Anal. Chem.*, 2016, **88**, 8323–8331.
49. N. Kurapati, D. C. Janda, R. J. Balla, S.-H. Huang, K. C. Leonard and S. Amemiya, *Anal. Chem.*, 2022, **94**, 17956–17963.
50. A. M. Najarian, R. Chen, R. J. Balla, S. Amemiya and R. L. McCreery, *Anal. Chem.*, 2017, **89**, 13532–13540.
51. R. Chen, A. M. Najarian, N. Kurapati, R. J. Balla, A. Oleinick, I. Svir, C. Amatore, R. L. McCreery and S. Amemiya, *Anal. Chem.*, 2018, **90**, 11115–11123.
52. B.-K. Kim, A. Boika, J. Kim, J. E. Dick and A. J. Bard, *J. Am. Chem. Soc.*, 2014, **136**, 4849–4852.
53. W. Cheng and R. G. Compton, *Angew. Chem. Int. Ed.*, 2014, **53**, 13928–13930.
54. J. Lee, Y. Kang, J. Chang, J. Song and B.-K. Kim, *ACS Sens.*, 2020, **5**, 1943–1948.
55. X. Li, S. Majdi, J. Dunevall, H. Fathali and A. G. Ewing, *Angew. Chem. Int. Ed.*, 2015, **54**, 11978–11982.
56. S. D. Kim, J. H. Park, H. Ahn, J. Lee, C.-H. Shin, W.-D. Jang, B.-K. Kim and H. S. Ahn, *Nanoscale*, 2022, **14**, 6981–6989.
57. B. M. Quinn, P. G. van't Hof and S. G. Lemay, *J. Am. Chem. Soc.*, 2004, **126**, 8360–8361.
58. J. Y. Lee, B.-K. Kim, M. Kang and J. H. Park, *Sci. Rep.*, 2016, **6**, 30022.
59. J. E. Dick, A. T. Hilterbrand, A. Boika, J. W. Upton and A. J. Bard, *Proc. Natl. Acad. Sci. U. S. A.*, 2015, **112**, 5303-5308.
60. J. E. Dick, A. T. Hilterbrand, L. M. Strawsine, J. W. Upton and A. J. Bard, *Proc. Natl. Acad. Sci. U. S. A.*, 2016, **113**, 6403-6408.
61. H. Deng, J. E. Dick, S. Kummer, U. Kragl, S. H. Strauss and A. J. Bard, *Anal. Chem.*, 2016, **88**, 7754–7761.
62. J. E. Dick, C. Renault, B.-K. Kim and A. J. Bard, *Angew. Chem. Int. Ed.*, 2014, **53**, 11859–11862.
63. R. Kazemi, N. E. Tarolla and J. E. Dick, *Anal. Chem.*, 2020, **92**, 16260–16266.
64. H. Deng, P. Peljo, X. Huang, E. Smirnov, S. Sarkar, S. Maye, H. H. Girault and D. Mandler, *J. Am. Chem. Soc.*, 2021, **143**, 7671–7680.
65. J. Zhang, L. Huang, T. Fang, F. Du, Z. Xiang, J. Zhang, R. Chen, P. Peljo, G. Ouyang and H. Deng, *ChemElectroChem*, 2022, **9**, e202200624.
66. J. Zhang, L. Huang, T. Fang, Z. Xiang, S. He, P. Peljo, S. Gan, X. Huang and H. Deng, *Chem. – An Asian J.*, 2022, **17**, e202200731.
67. T. Kakiuchi, *Electrochem. Commun.*, 2000, **2**, 317–321.
68. E. Laborda, A. Molina, V. F. Espín, F. Martínez-Ortiz, J. García de la Torre and R. G. Compton, *Angew. Chem. Int. Ed.*, 2017, **56**, 782–785.
69. A. Trojánek, V. Mareček and Z. Samec, *Electrochim. Acta*, 2020, **354**, 136653.
70. S. M. Oja, D. A. Robinson, N. J. Vitti, M. A. Edwards, Y. Liu, H. S. White and B. Zhang, *J. Am. Chem. Soc.*, 2017, **139**, 708–718.
71. C. C. Striemer, T. R. Gaborski, J. L. McGrath and P. M. Fauchet, *Nature*, 2007, **445**, 749–753.
72. K. Hill, S. N. Walker, A. Salminen, H. L. Chung, X. Z. Li, B. Ezzat, J. J. Miller, J. P. S. DesOrmeaux, J. K. Zhang, A. Hayden, T. Burgin, L. Piraino, M. N. May, T. R. Gaborski, J. A. Roussie, J. Taylor, L. DiVincenti, A. A. Shestopalov, J. L. McGrath and D. G. Johnson, *Adv. Healthcare Mater.*, 2020, **9**, 1900750.
73. A. A. Agrawal, B. J. Nehilla, K. V. Reisig, T. R. Gaborski, D. Z. Fang, C. C. Striemer, P. M. Fauchet and J. L. McGrath, *Biomaterials*, 2010, **31**, 5408–5417.
74. D. G. Johnson, T. S. Khire, Y. L. Lyubarskaya, K. J. P. Smith, J. P. S. DesOrmeaux, J. G. Taylor, T. R. Gaborski, A. A. Shestopalov, C. C. Striemer and J. L. McGrath, *Adv. Chronic Kidney Dis.*, 2013, **20**, 508–515.
75. H. H. Chung, M. Mireles, B. J. Kwarta and T. R. Gaborski, *Lab Chip*, 2018, **18**, 1671–1689.
76. E. Kim, H. Xiong, C. C. Striemer, D. Z. Fang, P. M. Fauchet, J. L. McGrath and S. Amemiya, *J. Am. Chem. Soc.*, 2008, **130**, 4230–4231.
77. F.-R. F. Fan and A. J. Bard, *Proc. Natl. Acad. Sci. U. S. A.*, 1999, **96**, 14222–14227.
78. D. T. Jantz, R. J. Balla, S.-H. Huang, N. Kurapati, S. Amemiya and K. C. Leonard, *Anal. Chem.*, 2021, **93**, 8906–8914.
79. P.-Y. Blanchard, T. Sun, Y. Yu, Z. Wei, H. Matsui and M. V. Mirkin, *Langmuir*, 2016, **32**, 2500–2508.
80. R. Ishimatsu, J. Kim, P. Jing, C. C. Striemer, D. Z. Fang, P. M. Fauchet, J. L. McGrath and S. Amemiya, *Anal. Chem.*, 2010, **82**, 7127–7134.
81. P. J. Rodgers, P. Jing, Y. Kim and S. Amemiya, *J. Am. Chem. Soc.*, 2008, **130**, 7436–7442.
82. Y. Yuan and S. Amemiya, *Anal. Chem.*, 2004, **76**, 6877–6886.
83. V. P. Menon and C. R. Martin, *Anal. Chem.*, 1995, **67**, 1920–1928.
84. A. J. Bard, L. R. Faulkner and H. S. White, *Electrochemical Methods: Fundamentals and Applications*, John Wiley & Sons, New York, 3rd ed., 2022, p. 275.
85. Y. Liu, J. Strutwolf and D. W. M. Arrigan, *Anal. Chem.*, 2015, **87**, 4487–4494.
86. L. Xie, X. Huang and B. Su, *ACS Sens.*, 2017, **2**, 803–809.
87. J. Guo and S. Amemiya, *Anal. Chem.*, 2006, **78**, 6893–6902.
88. Y. Kim and S. Amemiya, *Anal. Chem.*, 2008, **80**, 6056–6065.
89. Y. Kim, P. J. Rodgers, R. Ishimatsu and S. Amemiya, *Anal. Chem.*, 2009, **81**, 7262–7270.
90. B. Kabagambe, A. Izadyar and S. Amemiya, *Anal. Chem.*, 2012, **84**, 7979–7986.
91. B. Kabagambe, M. B. Garada, R. Ishimatsu and S. Amemiya, *Anal. Chem.*, 2014, **86**, 7939–7946.
92. M. B. Garada, B. Kabagambe, Y. Kim and S. Amemiya, *Anal. Chem.*, 2014, 11230–11237.
93. P. J. Greenawalt, M. B. Garada and S. Amemiya, *Anal. Chem.*, 2015, **87**, 8564–8572.
94. P. J. Greenawalt and S. Amemiya, *Ana. Chem.*, 2016, **88**, 5827–5834.
95. S. Amemiya, *Anal. Chem.*, 2016, **88**, 8893–8901.
96. C. Amatore, J. M. Savéant and D. Tessier, *J. Electroanal. Chem.*, 1983, **147**, 39–51.
97. A. Oleinick, O. Sliusarenko, I. Svir and C. Amatore, *J. Electrochem. Soc.*, 2020, **167**, 013530.
98. L. J. Terry, E. B. Shows and S. R. Wente, *Science*, 2007, **318**, 1412–1416.

99. A. Buchwalter, J. M. Kaneshiro and M. W. Hetzer, *Nat. Rev. Genet.*, 2019, **20**, 39–50.
100. S. Sakuma and M. A. D'Angelo, *Semin. Cell Dev. Biol.*, 2017, **68**, 72–84.
101. D. N. Simon and M. P. Rout, Cancer and the Nuclear Pore Complex in *Cancer Biology and the Nuclear Envelope: Recent Advances May Elucidate Past Paradoxes*, eds. E. C. Schirmer and J. I. DeLasHeras, 2014, vol. 773, pp. 285–307.
102. H. J. Kim and J. P. Taylor, *Neuron*, 2017, **96**, 285–297.
103. R. L. Adams and S. R. Wente, *Cell*, 2013, **152**, 1218–1221.
104. S. Amemiya, *Chem. Rec.*, 2021, **21**, 1430–1441.
105. J. Kim, A. Izadyar, M. Shen, R. Ishimatsu and S. Amemiya, *Anal. Chem.*, 2014, **86**, 2090–2098.
106. P. Pathirathna, R. J. Balla, G. Meng, Z. Wei and S. Amemiya, *Chem. Sci.*, 2019, **10**, 7929–7936.
107. J. Guo and S. Amemiya, *Anal. Chem.*, 2005, **77**, 2147–2156.
108. J. Kim, A. Izadyar, N. Nioradze and S. Amemiya, *J. Am. Chem. Soc.*, 2013, **135**, 2321–2329.
109. P. Pathirathna, R. J. Balla, D. T. Jantz, N. Kurapati, E. R. Gramm, K. C. Leonard and S. Amemiya, *Anal. Chem.*, 2019, **91**, 5446–5454.
110. P. Jing, P. J. Rodgers and S. Amemiya, *J. Am. Chem. Soc.*, 2009, **131**, 2290–2296.
111. D. Mohr, S. Frey, T. Fischer, T. Guttler and D. Görlich, *EMBO J.*, 2009, **28**, 2541–2553.
112. K. Ribbeck and D. Görlich, *EMBO J.*, 2002, **21**, 2664–2671.
113. A. Loschberger, S. van de Linde, M. C. Dabauvalle, B. Rieger, M. Heilemann, G. Krohne and M. Sauer, *J. Cell Sci.*, 2012, **125**, 570–575.
114. R. Chen, K. Xu and M. Shen, *Electrochim. Acta*, 2020, **357**, 136788.
115. H. D. Jetmore, C. B. Milton, E. S. Anupriya, R. Chen, K. Xu and M. Shen, *Anal. Chem.*, 2021, **93**, 16535–16542.
116. M. Zhou, Y. Yu, K. K. Hu and M. V. Mirkin, *J. Am. Chem. Soc.*, 2015, **137**, 6517-6523.
117. Z. G. Feng, N. S. Georgescu and D. A. Scherson, *J. Electrochem. Soc.*, 2017, **164**, H148–H152.
118. L. J. Colwell, M. P. Brenner and K. Ribbeck, *PLoS Comp. Biol.*, 2010, **6**, e1000747.
119. M. Tagliazucchi, O. Peleg, M. Kroger, Y. Rabin and I. Szleifer, *Proc. Natl. Acad. Sci. U. S. A.*, 2013, **110**, 3363–3368.
120. S. M. Paulillo, M. A. Powers, K. S. Ullman and B. Fahrenkrog, *J. Mol. Biol.*, 2006, **363**, 39–50.
121. X. Liu, M. M. Ramsey, X. Chen, D. Koley, M. Whiteley and A. J. Bard, *Proc. Natl. Acad. Sci. U. S. A.*, 2011, **108**, 2668–2673.
122. D. Koley, M. M. Ramsey, A. J. Bard and M. Whiteley, *Proc. Natl. Acad. Sci. U. S. A.*, 2011, **108**, 19996–20001.
123. J. Kim, J. L. Connell, M. Whiteley and A. J. Bard, *Anal. Chem.*, 2014, **86**, 12327–12333.
124. J. L. Connell, J. Kim, J. B. Shear, A. J. Bard and M. Whiteley, *Proc. Natl. Acad. Sci. U. S. A.*, 2014, **111**, 18255–18260.
125. D. P. Zhan, F. R. F. Fan and A. J. Bard, *Proc. Natl. Acad. Sci. U. S. A.*, 2008, **105**, 12118–12122.
126. K. B. Holt and A. J. Bard, *Biochemistry*, 2005, **44**, 13214–13223.
127. K. Rabaey and R. A. Rozendal, *Nat. Rev. Microbiol.*, 2010, **8**, 706–716.
128. D. R. Lovley, *Annu. Rev. Microbiol.*, 2012, **66**, 391–409.
129. E. Bakker, P. Bühlmann and E. Pretsch, *Chem. Rev.*, 1997, **97**, 3083–3132.
130. H. J. Lee, I. J. Yoon, C. L. Yoo, H.-J. Pyun, G. S. Cha and H. Nam, *Anal. Chem.*, 2000, **72**, 4694–4699.
131. R. Ishimatsu, A. Izadyar, B. Kabagambe, Y. Kim, J. Kim and S. Amemiya, *J. Am. Chem. Soc.*, 2011, **133**, 16300–16308.
132. N. Szeinbaum, H. Lin, J. A. Brandes, M. Taillefert, J. B. Glass and T. J. DiChristina, *Environ. Microbiol.*, 2017, **19**, 3475–3486.
133. P. Peljo and H. H. Girault, Liquid/Liquid Interfaces, Electrochemistry at. in *Encyclopedia of Analytical Chemistry*, ed R. A. Meyers, John Wiley & Sons, 2012, DOI: https://doi.org/10.1002/9780470027318.a5306.pub2.
134. H. R. Kim, C. M. Pereira, H. Y. Han and H. J. Lee, *Anal. Chem.*, 2015, **87**, 5356–5362.
135. B. Hribar, N. T. Southall, V. Vlachy and K. A. Dill, *J. Am. Chem. Soc.*, 2002, **124**, 12302–12311.
136. N. Kikkawa, L. Wang and A. Morita, *J. Am. Chem. Soc.*, 2015, **137**, 8022–8025.
137. S. G. Sabaragamuwe, D. Conti, S. R. Puri, I. Andreu and J. Kim, *Anal. Chem.*, 2019, **91**, 9599–9607.
138. S. G. Sabaragamuwe, H. Madawala, S. R. Puri and J. Kim, *Anal. Chim. Acta*, 2020, **1139**, 129–137.
139. H. Madawala, S. G. Sabaragamuwe, S. Elangovan and J. Kim, *Anal. Chem.*, 2021, **93**, 1154–1160.
140. X.-D. Wang, J. A. Stolwijk, T. Lang, M. Sperber, R. J. Meier, J. Wegener and O. S. Wolfbeis, *J. Am. Chem. Soc.*, 2012, **134**, 17011–17014.
141. C. M. Hill, J. Kim and A. J. Bard, *J. Am. Chem. Soc.*, 2015, **137**, 11321–11326.
142. P. Bühlmann, E. Pretsch and E. Bakker, *Chem. Rev.*, 1998, **98**, 1593–1688.
143. S. Amemiya and A. J. Bard, *Anal. Chem.*, 2000, **72**, 4940–4948.
144. X. Xie, G. Mistlberger and E. Bakker, *Anal. Chem.*, 2013, **85**, 9932–9938.
145. P. Molina, F. Zapata and A. Caballero, *Chem. Rev.*, 2017, **117**, 9907–9972.
146. S. Amemiya, P. Bühlmann, Y. Umezawa, R. C. Jagessar and D. H. Burns, *Anal. Chem.*, 1999, **71**, 1049–1054.
147. N. T. Iwai, M. Kramaric, D. Crabbe, Y. Wei, R. Chen and M. Shen, *Anal. Chem.*, 2018, **90**, 3067–3072.
148. R. Chen, A. B. McAllister and M. Shen, *J. Electroanal. Chem.*, 2020, **873**, 114303.
149. R. J. Balla, D. T. Jantz, N. Kurapati, R. Chen, K. C. Leonard and S. Amemiya, *Anal. Chem.*, 2019, 91, 10227–10235.
150. R. Gao, M. A. Edwards, J. M. Harris and H. S. White, *Curr. Opin. Electrochem.*, 2020, **22**, 170–177.
151. A. J. Schmeltzer, J. M. Harris and H. S. White, *ACS Nano*, 2023, **17**, 8829–8836.